Advances in Geo-Energy Research

Vol. 20, No. 1, p. 27-42, 2026

Original article

Full-field experimental investigation of heat transfer and thermoelastic response during steam injection into coal seam borehole

Yujie Li[1], Cheng Zhai[2], Liang Zhang[1,3],*, Honglian Li[4], Xianfeng Liu[5]

[1]*School of Emergency Management, Xihua University, Chengdu 610039, P. R. China*

[2]*School of Safety Engineering, China University of Mining and Technology, Xuzhou 221116, P. R. China*

[3]*Sichuan Highway Planning, Survey, Design and Research Institute Ltd., Chengdu 610041, P. R. China*

[4]*Faculty of Physics, University of Barcelona, Barcelona 08193, Spain*

[5]*State Key Laboratory of Coal Mine Disaster Dynamics and Control, Chongqing University, Chongqing 400044, P. R. China*

Keywords:
Steam injection
coalbed methane
digital image correlation
heat transfer
thermal stress

Cited as:
Li, Y., Zhai, C., Zhang, L., Li, H., Liu, X. Full-field experimental investigation of heat transfer and thermoelastic response during steam injection into coal seam borehole. Advances in Geo-Energy Research, 2026, 20(1): 27-42.
https://doi.org/10.46690/ager.2026.04.03

Abstract:
The accurate determination of thermal influence range during steam injection has long remained challenging in coal seam thermal stimulation, limiting the optimization of enhanced coalbed methane recovery strategies. Existing studies are primarily focused on the temperature variation of coal, while the thermal influence range and the spatial coupling between heat transfer and coal deformation have not been systematically quantified. This study presents a full-field experimental analysis of heat transfer and thermoelastic response during steam injection into a large-scale coal specimen with a prefabricated borehole. Infrared thermography and digital image correlation were employed to capture the spatiotemporal evolution of coal surface temperature and strain distributions, enabling the direct observation of their spatial correlation. The results underscore that saturated steam transfers energy predominantly through latent heat release, producing relatively uniform heating on coal, whereas superheated steam is dominated by sensible heat transfer and results in more heterogeneous temperature and strain distributions. Increasing the steam temperature or flow rate alone produce limited expansion of the thermal influence range. In contrast, enlarging the effective heat transfer area through fracture enhancement significantly promotes thermal propagation. A clear spatial correspondence between temperature and strain fields was identified, indicating that coal deformation is primarily governed by thermally induced stress within the observed deformation range. This paper provides a quantitative framework for the evaluation of steam-induced thermal influence range and thermoelastic coupling at the specimen scale, with the results providing a mechanistic basis for optimizing steam-assisted coal seam stimulation techniques.

1. Introduction

Coalbed methane (CBM) is an unconventional natural gas that has substantial energy value with significant environmental benefits (Moore, 2012; Zhang et al., 2025). It mainly consists of methane (typically accounting for 80% ~ 99% (Flores, 1998)) and is predominantly adsorbed within coal micropores. As a high-quality clean energy source, CBM has been extensively utilized in both residential and commercial gas supply (Gunter et al., 1997), industrial fuel (Qiu et al., 2024), power generation (Mallick and Prabu, 2017),

Yandy Scientific Press

*Corresponding author.
E-mail address: yujie_li@cumt.edu.cn (Y. Li); greatzc@cumt.edu.cn (C. Zhai); zthang_liang@xhu.edu.cn (L. Zhang); honglianli@ub.edu (H. Li); liuxf@cqu.edu.cn (X. Liu).

Received January 3, 2026; revised February 7, 2026; accepted February 28, 2026; available online March 3, 2026.

hydrogen production (Megía et al., 2021), and various other sectors. With the ongoing transition toward a low-carbon global energy structure and the imperative for cleaner production, the demand for CBM has been increasing steadily across many countries worldwide. Consequently, the exploration, development and utilization of CBM resources have become integral components of national energy strategies and reserves.

Currently, the predominant technique for CBM extraction is hydraulic fracturing combined with dewatering-induced pressure drawdown (Wei et al., 2025; Liang et al., 2025b). This conventional approach enhances coal seam permeability by generating fracture networks in coal seams through the injection of high-pressure aqueous fracturing fluids (Ma et al., 2024). Subsequent dewatering reduces reservoir pressure, thereby promoting methane desorption and migration. However, extensive fluid invasion frequently induces water-blocking (Verdugo and Doster, 2022) and irreversible formation damage (Zhang and Hascakir, 2021). Furthermore, this technique has limited applicability in low-water-saturation reservoirs, resulting in poor recovery efficiency. These issues have facilitated the development of advanced reservoir stimulation technologies, including liquid nitrogen fracturing (Longinos et al., 2025; Feng et al., 2026), liquid and supercritical CO_2 fracturing (Li et al., 2023; Yang et al., 2026), foam-based fracturing (Alarawi et al., 2023; Zheng et al., 2025b), gas injection (Talapatra et al., 2021; Liu et al., 2025), thermal stimulation (Liang et al., 2025a), and solvent-assisted extraction (Zheng et al., 2025a). Due to the strong adsorption capacity of CBM and the pronounced temperature sensitivity of the adsorption-desorption process (Pashin and McIntyre, 2003; Wang et al., 2025), thermal stimulation has attracted considerable research interest and emerged as a promising frontier in CBM production.

Thermal stimulation involves injecting high-temperature thermal media, such as hot water, heated gases (N_2 or CO_2) or steam, into the coal seam, or applying in-situ heating via electromagnetic methods (microwave or radiofrequency (Lan et al., 2021; Tang et al., 2024)) or electrical resistance heating (Shahtalebi et al., 2016). With rising formation temperature, the methane adsorption capacity decreases while the desorption rate correspondingly increases (Zhao et al., 2022). Because steam has excellent thermal transport properties, it has been widely employed in the recovery of heavy oil and bitumen resources (Gong et al., 2022), with its associated technologies and equipment reaching a relatively mature stage. In recent years, steam has demonstrated significant potential for enhancing CBM recovery. Both experiments and numerical simulations have shown that steam stimulation can significantly increase methane production compared with conventional extraction methods (Hu et al., 2023; Nie, 2023), highlighting its technical feasibility. Compared with hot water and other thermal fluids, steam exhibits lower heat loss and higher thermal utilization efficiency, making it attractive for low-permeability coal seams.

When steam is injected into coal seams, the immediate response is a rapid rise in coal temperature, which in turn reduces its methane adsorption capacity, induces thermal deformation, and alters the structure and physicochemical properties. Consequently, the effectiveness of steam-assisted CBM recovery largely depends on the spatial extent of heat propagation within the seam. The magnitude and distribution of the high-temperature region directly affect methane desorption intensity and the development of methane seepage pathways.

At present, research on heat transfer in coal during thermal stimulation is dominated by numerical simulations. Various models have been developed to characterize temperature evolution and multi-field interactions around injection boreholes (Teng et al., 2018; Yuan et al., 2019). More advanced formulations incorporating fracture-fluid interactions and conjugate heat transfer processes have further refined the representation of heterogeneous coal structures (Liu et al., 2023, 2024). These studies have provided important theoretical insights into the governing mechanisms of heat propagation in coal; however, most simulations have relied on idealized material assumptions and simplified structural representations, and their predictive reliability is often constrained by limited experimental validation, particularly at larger spatial scales.

A number of experimental investigations have complemented numerical studies by directly observing temperature responses under steam injection. Infrared thermography and triaxial testing have been utilized to characterize temperature evolution and methane production behavior in coal specimens of varying sizes (Li et al., 2018, 2022). Thus, the influence of maceral composition, fracture distribution and injection conditions on heat transfer efficiency were revealed. Nevertheless, most of these experiments were conducted on relatively small specimens, restricting the representation of in situ heterogeneity and scale effects. In addition, prior experimental work has primarily focused on the temperature variation itself, whereas attempts have been relatively scarce to quantitatively characterize of the thermal influence range and its coupling with deformation behavior.

A synthesis of existing studies indicates that, although both modeling and laboratory experiments have advanced our understanding of thermal stimulation in coal seams, distinct challenges remain. First, the large-scale experimental validation of coupled heat transfer and deformation processes is still insufficient. Second, the spatial expansion of the thermal influence range has been rarely quantified systematically. Third, the interaction between temperature gradients and strain evolution has not been comprehensively evaluated under conditions representative of borehole steam injection.

To address these gaps, this study conducted a full-field experimental investigation using a large coal block (600 mm in length) containing a prefabricated semi-borehole structure to better approximate field conditions. Infrared thermography and digital image correlation (DIC) were employed to monitor the spatiotemporal evolution of coal surface temperature and strain fields during steam injection. Systematically controlling the steam flow rate, steam temperature and effective heating area of the coal allowed quantitatively evaluating the thermal influence range of steam and clarifying the thermoelastic response behavior of coal. The findings aim to provide a more robust experimental basis for optimizing steam-assisted coal seam stimulation strategies.

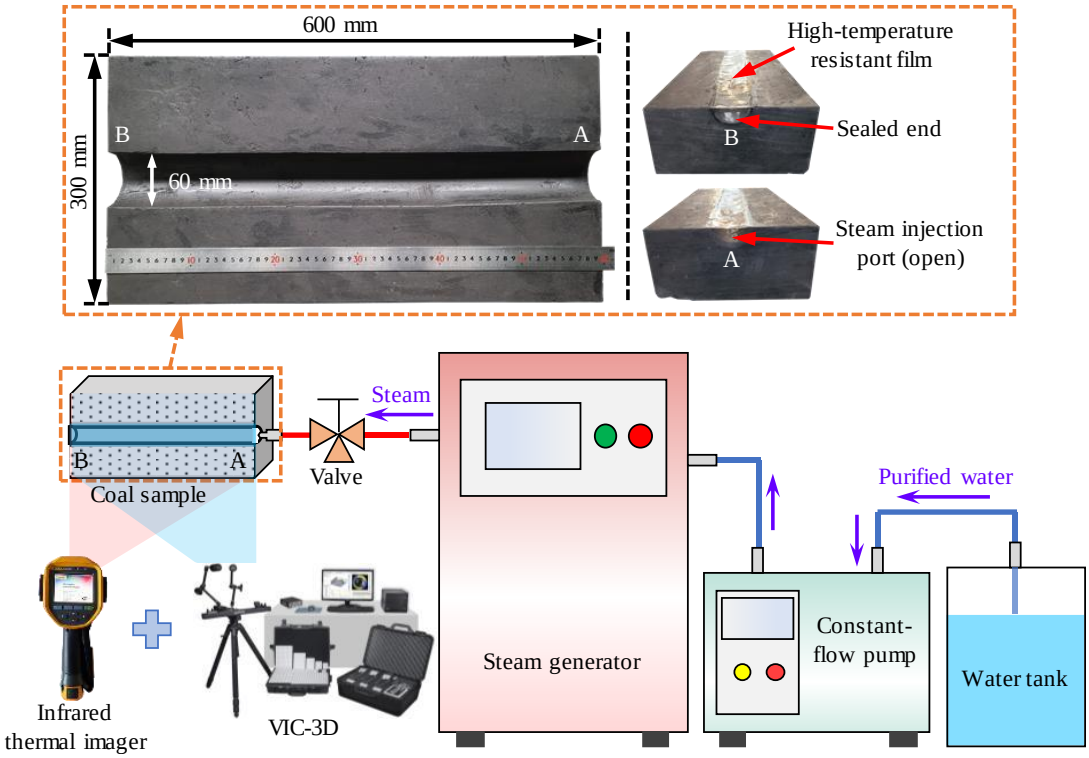

Fig. 1. Schematic diagram of the experimental system.

Table 1. Results of proximate analysis and microscopic component analysis of the coal sample.

$R_{o,\max}$	Proximate analysis (wt.%)				Maceral analysis (vol.%)			
	M_{ad}	A_{ad}	V_{ad}	C_{ad}	V	I	E	M
0.53	10.09	8.42	25.68	55.81	17.51	74.94	1.01	6.54

Notes: M_{ad}: Moisture, air-drying basis; A_{ad}: Ash yield, air-drying basis; V_{ad}: Volatile matter, air-drying basis; C_{ad}: Fixed carbon content, air-drying basis; $R_{o,\max}$: Maximum reflectance of vitrinite; V: Vitrinite; I: Inertinite; E: Exinite; M: Minerals.

2. Experimental materials and methods

2.1 Materials

The coal samples used in this study were collected from the Hongyan Coal Mine in Shaanxi Province, China. After transporting large raw blocks to the laboratory, one was cut into a rectangular specimen measuring 600 mm in length, 150 mm in width and 300 mm in height using a precision cutting machine. As illustrated in Fig. 1, a semi-cylindrical borehole with a diameter of 60 mm was drilled along the longitudinal centerline of the sample surface. A layer of high-temperature-resistant, waterproof transparent film was then adhered to the borehole surface to form a steam flow channel. To prevent steam or condensate leakage, a flexible high-temperature waterproof sealant was applied at the junction between the film and the coal surface. One end of the borehole remained open for steam injection (marked A), while the opposite end was sealed (marked B) to simulate bottom-hole steam injection in field applications. This configuration increases steam residence time within the borehole, promotes internal recirculation and mixing, and enhances heat exchange between the steam and the borehole wall. Furthermore, it prevents direct through-flow and rapid steam escape, thereby better representing confined thermal stimulation conditions in coal seams.

To determine the basic physicochemical parameters of the coal, several small coal fragments were crushed and subjected to proximate analysis, vitrinite reflectance measurements, and maceral composition analysis. The results are summarized in Table 1.

2.2 Experimental system and apparatus

The experimental system comprises three main subsystems: The steam injection system, the temperature field acquisition system, and the VIC-3D (video image correlate, 3D) non-contact full-field strain measurement system (hereinafter referred to as “VIC-3D”), as shown in Fig. 1.

The steam injection system consists of a steam generator, a water tank, purified water, a constant-flow pump, and connecting pipelines. The temperature field acquisition system includes an infrared thermal imager and associated analytical software. The VIC-3D is composed of two high-speed charge-coupled device (CCD) cameras, a camera bracket, light-emitting diode (LED) light sources, a data acquisition processor, a computer, image analysis software, a calibration plate, and a speckle-pattern preparation kit. Detailed descriptions of the individual systems and instruments are provided below.

(1) Steam generator

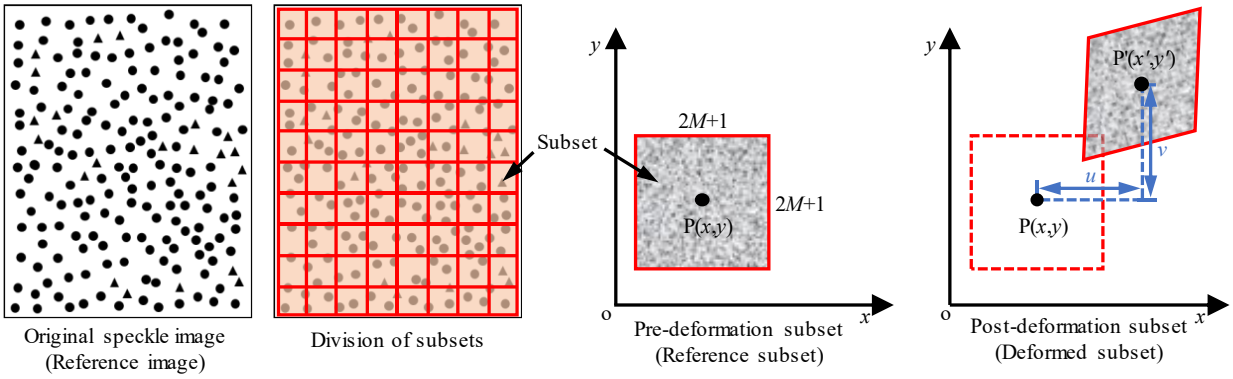

Fig. 2. Schematic diagram of the calculation principle of DIC.

The steam generator (HAGFQ-15L, Hua'an Scientific Instruments Co., Ltd., Jiangsu, China) was used to produce steam at various temperatures and flow rates. This component has a total heating power of 24 kW, a maximum heating temperature of 550 °C, and a pressure tolerance of 10 MPa. To effectively limit heat loss, glass wool insulation was applied to the steam transport pipelines.

(2) Constant-flow pump

A constant-flow pump (Y-1000, Hua'an Scientific Instruments Co., Ltd., Jiangsu, China) was employed to deliver purified water into the steam generator. The pump has a maximum flow rate of 300 mL/min with a precision of 0.1 mL/min and a pressure tolerance of 10 MPa. This device enables precise control of the water input, thereby ensuring accurate regulation of steam flow rate.

(3) Infrared thermal imager

An infrared thermal imager (Ti450, Fluke Corporation, USA) was utilized to capture the surface temperature distribution of the coal samples. The measurement range of the device is from -20 to +1,200 °C, with an accuracy of ±2 °C and a thermal sensitivity of ≤ 0.03 °C.

(4) VIC-3D

The VIC-3D (Correlated Solutions Inc., USA) was employed to obtain full-field three-dimensional displacement and strain data. The system is capable of measuring strain and displacement in the range of 0.005% to over 2,000%, with a maximum CCD camera acquisition frequency of 43 Hz.

The VIC-3D determines strain based on the DIC technique, which calculates displacement and strain by comparing the grayscale distribution of image subsets before and after deformation. The fundamental principle involves selecting a subset centered on a target point in the undeformed speckle image (referred to as the reference subset) and searching for the corresponding subset in the deformed image (the deformed subset) using a predefined correlation function. The displacement and strain of each point are then derived from the positional and shape changes of the subset between the two images. By repeating this process for all subsets, a full-field displacement and strain map can be obtained (Wang et al., 2015).

In two-dimensional analysis, the undeformed and deformed images are defined as the reference and deformed images, respectively, as illustrated in Fig. 2. A subset centered at point $\mathrm{P}(x,y)$ with a size of $(2M+1)\times(2M+1)$ pixels is selected in the reference image. Using a correlation function and search algorithm, the corresponding subset centered at point $\mathrm{P}'(x',y')$ in the deformed image is identified to determine the displacement components u and v along the x and y directions, respectively (Hassan, 2021). The correlation between the reference and deformed subsets is quantified using a predefined criterion. Among several available criteria, the Zero-mean Normalized Cross-Correlation (ZNCC) has been adopted most widely due to its robustness against noise and insensitivity to illumination variations. The ZNCC coefficient, C, is given by Hassan (2021):

$$C=\sum_{i=-M}^{M}\sum_{j=-M}^{M}\frac{[f(x_i,y_j)-f_m]\left[g(x_i',y_j')-g_m\right]}{\Delta f\Delta g} \tag{1}$$

where C represents the correlation coefficient, $2M+1$ denotes the length of the side of the subset, $f(x_i,y_j)$ and $g(x_i',y_j')$ represent the grayscale values at the ith, jth pixel in the reference and deformed subsets, respectively, while f_m and g_m denote their average grayscale values; Δf and Δg are respectively the sets of grayscale deviations obtained after the zero-mean processing of all pixels in the reference and deformed subsets. The calculations for f_m, g_m, Δf and Δg are as follows:

$$f_m=\frac{1}{(2M+1)^2}\sum_{i=-M}^{M}\sum_{j=-M}^{M}f(x_i,y_j) \tag{2}$$

$$g_m=\frac{1}{(2M+1)^2}\sum_{i=-M}^{M}\sum_{j=-M}^{M}g(x_i',y_j') \tag{3}$$

$$\Delta f=\sqrt{\sum_{i=-M}^{M}\sum_{j=-M}^{M}[f(x_i,y_j)-f_m]^2} \tag{4}$$

$$\Delta g=\sqrt{\sum_{i=-M}^{M}\sum_{j=-M}^{M}\left[g(x_i',y_j')-g_m\right]^2} \tag{5}$$

When the two subsets are fully correlated, the correlation coefficient equals to 1. Deformation reduces this value, allowing the displacement to be determined by locating the point corresponding to the maximum correlation coefficient.

2.3 Experimental procedure

To investigate the thermal behavior of coal under representative steam injection conditions, two typical temperature levels were selected. Saturated steam at 100 °C was chosen as a baseline condition corresponding to atmospheric-pressure steam, which allows stable and controllable laboratory operation and represents a latent heat-dominated heat transfer mode. Superheated steam at 200 °C was selected to simulate a higher-temperature injection scenario with increased sensible heat contribution. This temperature level remains below the threshold of thermal decomposition of coal while providing a larger thermal gradient, enabling a clearer observation of temperature field evolution and thermoelastic response.

This study first conducted an experiment of injecting saturated steam at 100 °C according to the following experimental procedure:

1) The coal specimen was placed on the sample platform, and the steam injection end was aligned with the outlet of the steam generator.
2) The initial surface temperature distribution of the coal sample was recorded using the infrared thermal imager.
3) The steam generator was powered on and heated until the internal chamber temperature reached 120 °C and stabilized (corresponding to a steam outlet temperature of approximately 100 °C). The constant-flow pump was then activated to inject purified water into the steam generator at a flow rate of 50 mL/min, producing saturated steam. The outlet temperature was monitored in real time. Once both the steam temperature and the flow rate stabilized, the steam was injected into the borehole.
4) Infrared thermal images of the coal surface were captured every 5 min for a total duration of 90 min, yielding a time-resolved temperature field dataset.
5) After each experiment, the specimen was cooled for 24 to 48 h before repeating steps 1 to 4. Two additional tests were performed with steam flow rates of 100 mL/min and 150 mL/min, respectively, while maintaining other conditions unchanged.

Following the above tests, experiments using superheated steam at 200 °C were conducted to simultaneously monitor the temperature and strain fields on the coal surface. The specific procedure was as follows:

1) Based on the previous sample preparation procedure (Section 2.1), the surface of the coal sample was uniformly coated with a layer of matte white paint to serve as a background for strain measurement. After air-drying, a random black speckle pattern was applied using a speckle-generation tool.
2) The specimen was placed on the sample platform, with the borehole aligned to the steam outlet of the generator. The VIC-3D was set up and adjusted, so that the center of the sample was aligned with the optical axis of the cameras. The lens focus and exposure were tuned until most of the speckle-covered area appeared purple in the preview, indicating optimal illumination. Calibration was then performed using the VIC-Snap software: A calibration plate was photographed at multiple angles and positions, yielding no fewer than 30 calibration images. The results were imported into the calibration module for evaluation, and a calibration score below 0.05 indicated satisfactory accuracy.
3) The initial surface temperature of the coal sample was captured using the infrared thermal imager.
4) The internal heating chamber of the steam generator was set to 230 °C, corresponding to an outlet temperature of approximately 200 °C. The constant-flow pump was adjusted to a flow rate of 50 mL/min, and the steam was injected following the same procedure as described above.
5) Upon the initiation of steam injection, the VIC-3D immediately began image acquisition at a frequency of 0.1 Hz. Simultaneously, the infrared thermal imager was used to record surface temperature distributions every 5 min for a total of 90 min.

3. Results

3.1 Changes in the surface temperature field of coal

To characterize the spatiotemporal evolution of heat propagation during steam injection, the surface temperature distribution of the coal specimen was systematically analyzed under saturated steam conditions with varying flow rates and injection durations. Particular attention was given to the development of the high-temperature region and the temperature response of representative zones within the specimen. Fig. 3 illustrates the evolution of the surface temperature field of the coal and the corresponding central temperature of different regions during steam injection. Upon the initiation of steam injection, the coal surface temperature increased progressively and the resulting high-temperature region expanded outward from the borehole. However, a clear temperature asymmetry between the upper and lower regions of the specimen could be observed throughout the heating process. When the steam flow rate was 50 mL/min, the central temperature of Region 1 increased by 8.5, 12.8 and 14.4 °C after 30, 60 and 90 min of injection, respectively (with an initial coal temperature of approximately 17.7 °C). In contrast, the corresponding temperature increases in Region 2 were only 3.1, 5.7 and 8.7 °C. As the steam flow rate increased, the overall surface temperature field exhibited negligible variation. The central temperatures in Regions 1 and 2 increased slightly. For example, after 90 min of steam injection, the central temperature of Region 1 at flow rates of 100 and 150 mL/min was merely 0.2 and 0.3 °C higher than that at 50 mL/min, respectively. This is primarily attributed to the asymmetric heat transfer above and below the borehole.

To evaluate the overall temperature evolution of coal, the average temperatures of the upper and lower regions were calculated using SmartView software. As presented in Fig. 4(a), the average temperature of the coal increased steadily with steam injection time, while Region 1 consistently remained at a higher temperature than Region 2. During the initial 5 min, the surface temperature of the coal rose rapidly, followed by a gradual decline in the temperature increase rate. After 90

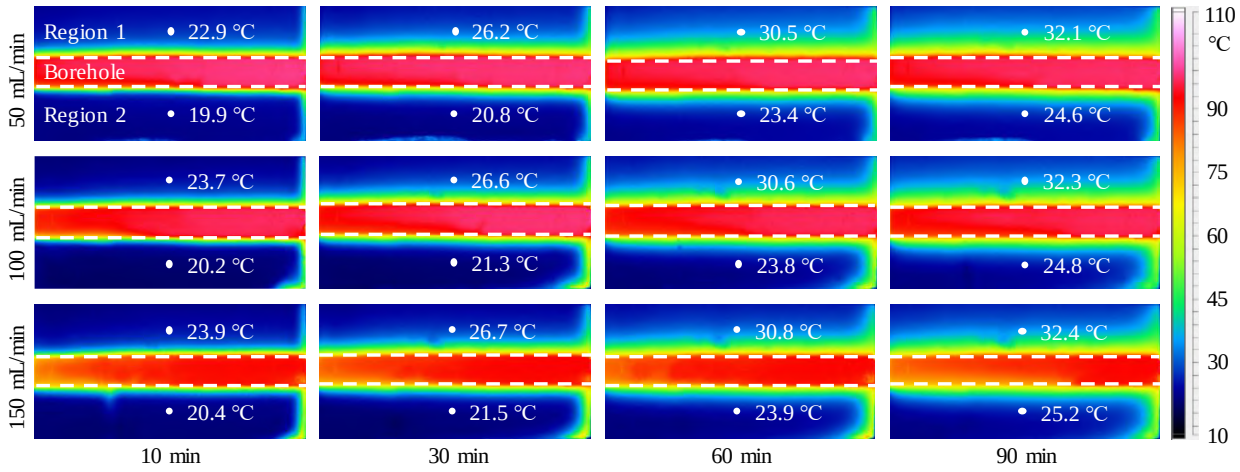

Fig. 3. Changes in coal surface temperature field at different durations of saturated steam injection into the borehole.

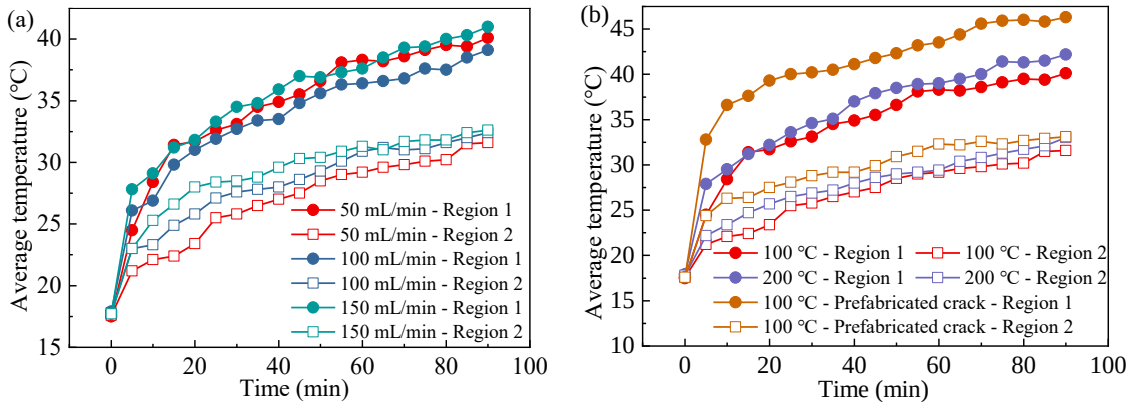

Fig. 4. Changes in the average temperatures of different areas on the coal surface with steam injection time: (a) Saturated steam injection and (b) steam injection at flow rate of 50 mL/min.

min of steam injection, the average temperatures of Region 1 increase by 22.6, 21.2 and 23.3 °C at steam flow rates of 50, 100 and 150 mL/min, respectively, while those of Region 2 increase by 14.0, 14.6 and 14.9 °C, respectively. The results suggest that within the tested flow range ($\leq$ 150 mL/min), the steam flow rate had a limited effect on the heat transfer range.

To quantify the heat transfer range of steam, regions where the surface temperature exceeded 40 °C (i.e., about 20 °C higher than the initial temperature) were defined as high-temperature regions. Using SmartView, these regions were highlighted in white (Fig. 5(a)), and then these images were analyzed using MATLAB for grayscale and binary processing. Subsequently, the proportion of the white area relative to the total surface area (including the borehole) was calculated to characterize the evolution of the high-temperature region.

The above image processing approach enables a clearer identification of the spatial extent of high-temperature region and facilitates comparison under different injection durations. As shown in Fig. 5(b), the high-temperature region expanded progressively with increasing steam injection time, exhibiting a pattern characterized by rapid expansion in the early stages followed by gradual stabilization. For instance, at a steam flow rate of 50 mL/min, the high-temperature region increased by 7.9% between 10 and 30 min (0.395%/min on average) and by 9.86% between 30 and 90 min (0.164%/min), indicating a significant slowdown in expansion. Moreover, as the steam flow rate increased, the overall expansion of the high-temperature region became slightly more pronounced, though the increment remained small. For example, during 10 and 60 min of steam injection, the high-temperature region expanded by 13.66%, 14.40% and 16.89% at flow rates of 50, 100 and 150 mL/min, respectively.

In summary, the development of the coal surface temperature field during saturated steam injection at 100 °C exhibited the following characteristics: (1) A rapid initial temperature rise within the first 10 min followed by a gradual slowdown; (2) a persistent thermal asymmetry between the upper and lower regions, with the upper region being approximately 6 $\sim$ 10 °C warmer due to condensate accumulation on the lower borehole wall; and (3) an overall weak dependence of the heat transfer range on steam flow rate, as increasing the steam flow rate from 50 to 150 mL/min caused only minor changes in the surface temperature distribution and the high-temperature area ratio.

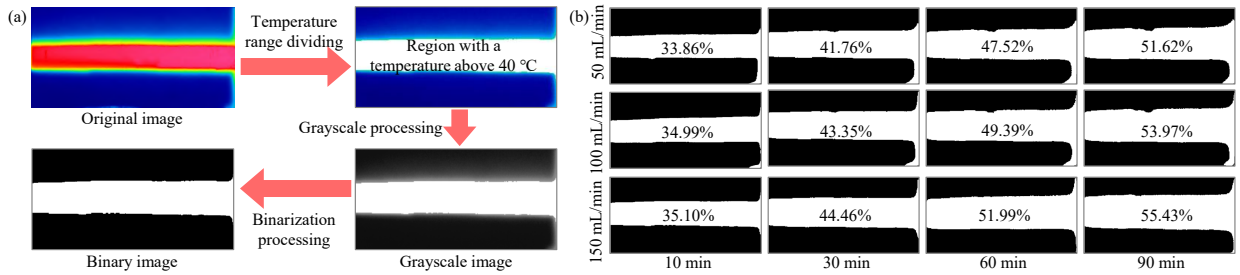

Fig. 5. (a) Image processing steps of the coal surface temperature field and (b) binary images of the coal surface temperature field and the proportion of high-temperature region at different durations of saturated steam injection into the borehole.

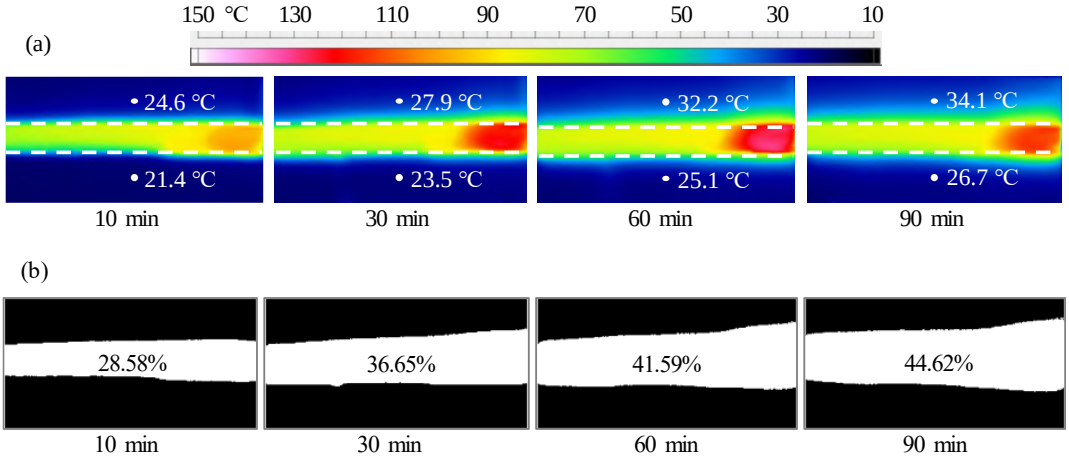

Fig. 6. Changes in the (a) coal surface temperature field and (b) high-temperature region at different durations of superheated steam injection into the borehole.

Subsequent to the results obtained under saturated steam injection, the thermal response of coal under superheated steam conditions was presented for comparison. This allowed an assessment of how the steam thermodynamic state influences temperature evolution and spatial distribution. Fig. 6(a) shows the evolution of the surface temperature field and the corresponding central temperatures of Regions 1 and 2 during superheated steam injection at 200 °C. The coal surface temperature increased gradually with steam injection time, accompanied by noticeable differences in spatial distribution compared with the saturated steam case. After 30, 60 and 90 min of steam injection, the central temperatures of Region 1 increased by 10.1, 14.4 and 16.3 °C, respectively (with an initial temperature of 17.8 °C), while the corresponding increases in Region 2 were 5.7, 7.3 and 8.9 °C. Compared with the results in Fig. 3, the enhancement in central temperature caused by superheated steam was only 0 ~ 2 °C greater than that produced by saturated steam.

To further evaluate the overall thermal response of coal, the average temperatures of the two regions were calculated using the method described above. The results shown in Fig. 4(b) indicate that superheated steam induced only a marginally higher temperature rise than saturated steam. After 10, 30, 60, and 90 min of steam injection, the average temperatures in Region 1 increased by 11.6, 16.7, 21.1, and 24.3 °C, respectively, which were only 0 ~ 3 °C higher than those under saturated steam. Similarly, the average temperatures in Region 2 increased by 5.6, 9.1, 11.6, and 15.2 °C, representing differences of merely 0 ~ 2 °C.

To analyze the variation in the heat transfer range, the regions with surface temperatures above 40 °C were defined as high-temperature regions, and the corresponding binary images and area ratios were shown in Fig. 6(b). The results indicate that the high-temperature region also expanded gradually with time under superheated steam injection, while the extent of expansion was smaller than that observed for saturated steam. For example, from 10 to 90 min, the high-temperature region expanded by 17.76% under saturated steam and by 16.04% under superheated steam at a steam flow rate of 50 mL/min. Furthermore, the high-temperature region was more concentrated near the steam injection end (right-hand side) under superheated steam conditions, whereas the saturated steam case exhibited a more uniform temperature distribution along the borehole axis. The localized high-temperature regions near the upper-right and lower-right corners were primarily caused by escaping steam and condensate accumulation and could be neglected in the overall assessment.

3.2 Changes in the surface strain field of coal

Based on the observed temperature field evolution, the corresponding deformation behavior of the coal sample was further analyzed to evaluate its thermoelastic response under superheated steam injection. Particular attention was given to

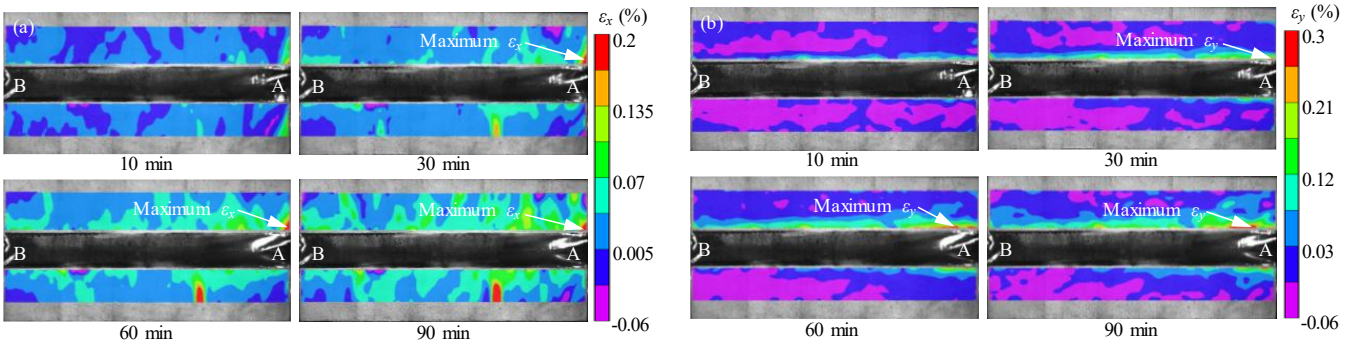

Fig. 7. Changes in (a) transverse strain field and (b) longitudinal strain field on the surface of the coal sample.

the strain distribution in regions adjacent to the borehole, where temperature gradients were most pronounced. Figs. 7(a) and 7(b) illustrate the evolution of the transverse and longitudinal surface strain fields of the coal sample during superheated steam injection. In the strain maps, positive and negative values represent tensile and compressive deformation, respectively.

When steam was injected into the borehole, both the transverse strain (ε_x) and longitudinal strain (ε_y) of the coal surface were predominantly positive, with only localized compressive zones, indicating an overall tensile deformation with localized compression. Moreover, the strain field exhibited a non-uniform distribution. After 10 min of steam injection, most regions of the coal surface exhibited a transverse strain below 0.0375%, while localized areas near the steam inlet reached 0.07% $\sim$ 0.135%. The majority of the longitudinal strain remained below 0.03%, with the region above the borehole near the steam injection port showing local strain values between 0.03% and 0.12%. As the steam injection proceeded, both ε_x and ε_y gradually increased. After steam injection for 90 min, the transverse strain over most of the surface ranged between 0.0375% and 0.07%, with higher strain (0.07% $\sim$ 0.135%) concentrated in the upper region near the borehole and strain values decreased with distance from the steam injection end. A similar trend was observed for ε_y, with the upper coal region exhibiting greater strain than the lower region, and regions near the borehole showing higher deformation than those farther away.

To further elucidate the strain evolution, six reference points were selected on the coal surface, as shown in Fig. 8(a). Figs. 8(b) to 8(e) present the temporal variations of ε_x and ε_y at these locations (the raw strain data were smoothed due to small magnitude and noise, allowing for a clearer view). The results demonstrate that both ε_x and ε_y at P_3 increased rapidly during the early steam injection stage and then stabilized, indicating a rapid initial tensile response followed by steady-state deformation. After 90 min of steam injection, ε_x at P_3 exceeded ε_y by approximately 0.167%. At P_1 and P_2, both ε_x and ε_y exhibited rapid early-stage increases followed by slower growth, though ε_x was slightly smaller than ε_y, with the differences being 0.056% and 0.118% at 90 min, respectively. At P_4, ε_x increased rapidly to about 0.13% and then stabilized, while ε_y increased only slightly to about 0.025% before remaining constant. At P_5 and P_6, the magnitudes and evolution patterns of ε_x were similar, indicating minor horizontal deformation characterized by initial tension and subsequent mild compression. The longitudinal strains at these points rose slightly and then stabilized.

By comparing the strain variations at different points, the following patterns could be identified: (1) Along the horizontal direction, for coal above the borehole, the longitudinal strain decreases with increasing distance from the injection port ($P_3 > P_2 > P_1$), while the transverse strain near the upper borehole bottom is slightly greater than that near the mid-borehole region ($P_3 > P_1 > P_2$); (2) along the vertical direction, the transverse strain above the borehole decreases with distance from the inlet ($P_3 > P_4 > P_5$); (3) the strain above the borehole is substantially greater than that below ($P_3 > P_6$).

3.3 Comparison between surface temperature and strain fields

Under the present experimental conditions, surface deformation of the coal is predominantly governed by thermally induced expansion associated with steam injection. Therefore, the spatial and temporal evolution of the strain field is expected to be closely related to the temperature distribution. As shown in Fig. 9, a clear spatial correspondence was observed between the longitudinal strain field and the surface temperature field, with regions of elevated temperature generally coinciding with higher tensile strain values.

To quantitatively examine the correlation between temperature evolution and strain response, the temperature evolution at monitoring point P_3 was extracted and compared with the corresponding strain values (ε_x and ε_y), as shown in Fig. 10(a). In addition, the average surface temperature of the coal was calculated and correlated with the corresponding average strain values (average ε_x and ε_y), as presented in Fig. 10(b). To further evaluate the strength and consistency of these relationships, correlation heat maps were constructed in both Figs. 10(a) and 10(b), providing a visual representation of the degree of statistical association between temperature and strain.

The results indicate that the transverse strain (ε_x), longitudinal strain (ε_y), and temperature at monitoring point P_3 exhibited a similar overall temporal evolution, characterized

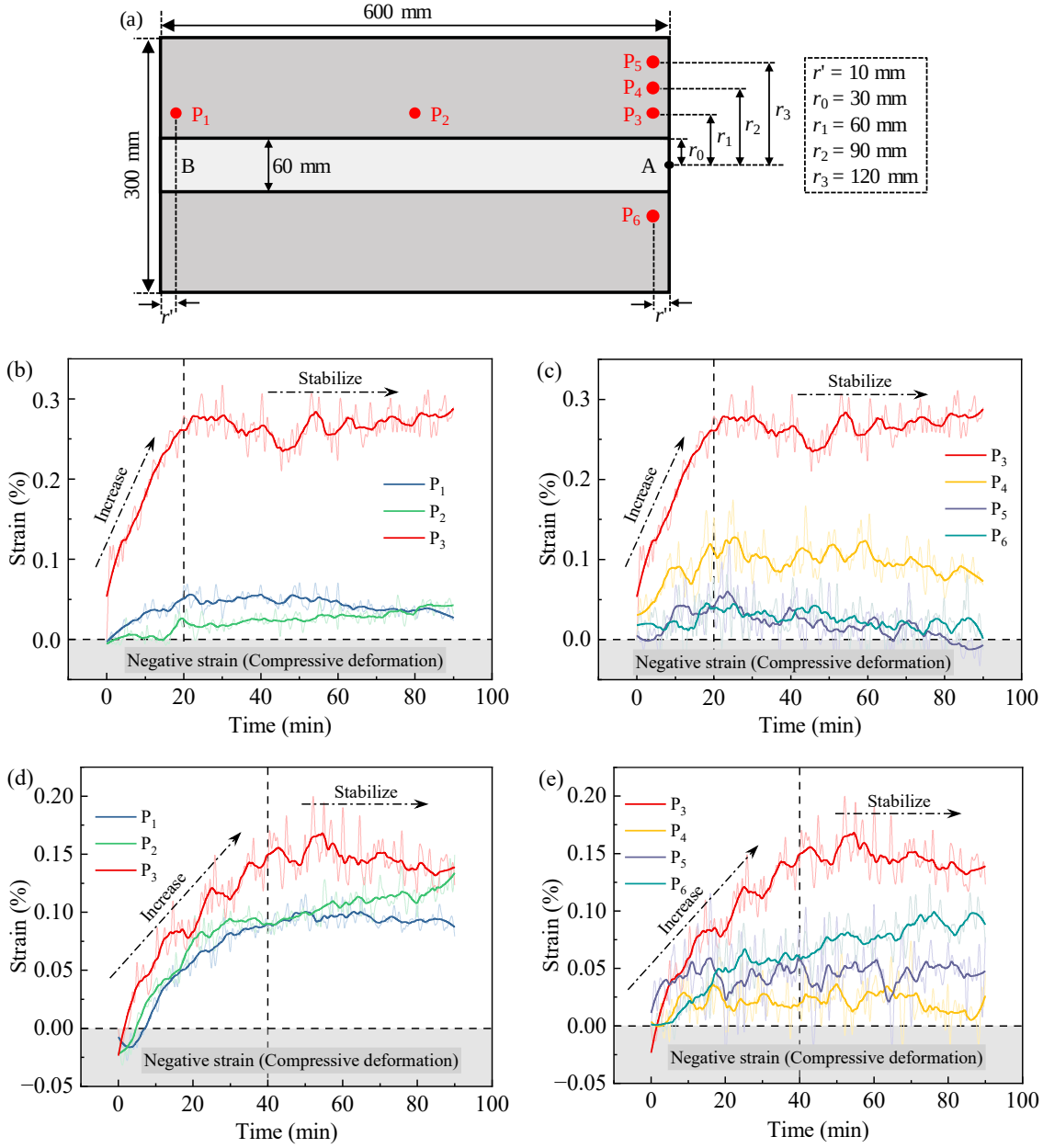

Fig. 8. (a) Schematic diagram of the location of reference points, (b)-(c) variation in transverse strains at each reference point and (d)-(e) variation in longitudinal strains at each reference point with the steam injection time.

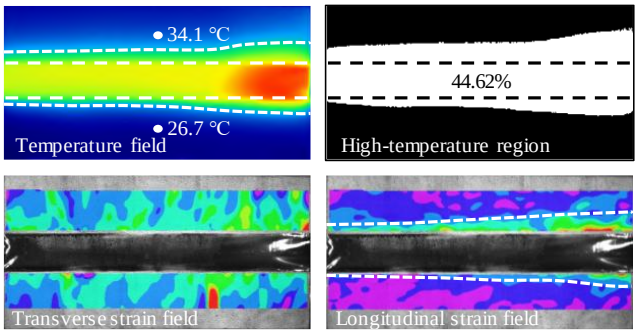

Fig. 9. Temperature field, high-temperature region, lateral strain field, and longitudinal strain field of the coal surface after 90 min of superheated steam injection into the borehole.

by a rapid increase during the initial stage of steam injection followed by gradual stabilization. However, their rates of increase differed. The transverse strain increased sharply within the first 20 min, reaching a plateau earlier than both the temperature and longitudinal strain. The longitudinal strain showed a rapid increase during the first 40 min before stabilizing, whereas the temperature continued to rise over approximately 50 min prior to approaching a steady state.

The correlation heat maps further demonstrated a strong statistical association between temperature and both strain components at P_3. Among them, ε_y exhibited a slightly stronger temporal correlation with temperature variations. At the specimen scale, the spatially averaged transverse strain showed a closer relationship with the overall average surface

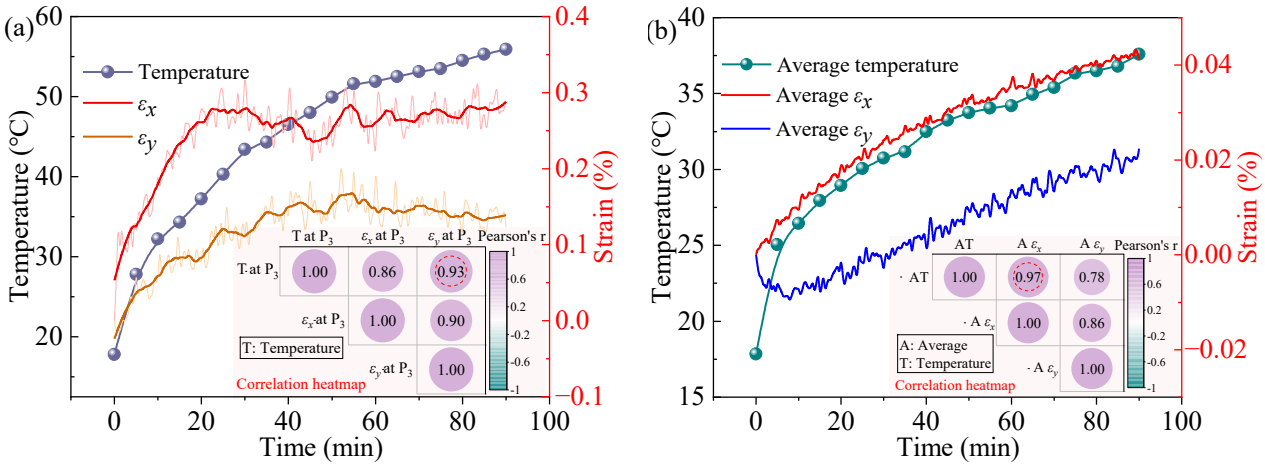

Fig. 10. (a) Temperature and strain changes at P_3 and their correlations and (b) changes in average surface temperature and average strain of coal and their correlations during steam injection into the borehole at different time points.

temperature compared with the longitudinal strain, indicating scale-dependent differences in the thermoelastic response behavior.

4. Discussion

4.1 Enhanced heat exchange methods

The experimental results indicate that increasing the steam flow rate (50 ~ 150 mL/min) or temperature (100 ~ 200 °C) produced only limited enhancement of coal surface temperature distribution and thermal influence range. After 90 min of injection, variations in central temperature and the extent of the high-temperature region in both the upper and lower regions remained marginal. These results suggest that within the tested parameter range, simply intensifying injection conditions was insufficient to substantially improve heat transfer in coal.

Previous studies have demonstrated that fracture networks significantly alter heat transfer behavior in porous media. Jarrahi et al. (2019) found that discrete fracture models predict higher thermal transport efficiency than equivalent homogeneous porous media, primarily because fractures enhance convective heat exchange and increase the effective heat transfer area. In contrast, heat transport in non-fractured media is more diffusion-dominated, resulting in slower thermal propagation and smoother temperature gradients. Heinze and Pastore (2023) further emphasized the velocity-dependent nature of heat transfer in fractured systems, where flow rate and fracture aperture strongly influence local heat transfer coefficients, leading to rapid and spatially heterogeneous temperature evolution. Similarly, Mezon et al. (2018) demonstrated that fractures promote stronger convective circulation even when effective bulk properties are comparable to those of homogeneous media. These findings indicate that fracture development can substantially enhance convective heat transfer and accelerate thermal propagation.

According to Newton's law of cooling (Nandagopal, 2023), the total heat transfer rate is proportional to the heat transfer area when other parameters remain constant. Therefore, enlarging the effective heat exchange area may provide a more efficient approach to improving thermal propagation in coal. To verify this hypothesis, the previously tested coal block was reprocessed to introduce artificial fractures around the borehole. Ten fractures were symmetrically cut using a precision cutting saw, as shown in Fig. 11(a). Each fracture measured 100 mm in length, 5 mm in width and 20 mm in depth, with a spacing of 100 mm. These prefabricated cracks were designed to simulate natural cleats and bedding fractures commonly present in coal seams. After removing coal dust, the borehole and fracture surfaces were sealed with a high-temperature-resistant waterproof film, keeping one end of the borehole open and the other sealed. A saturated steam injection test (50 mL/min) was then conducted following the procedure described in Section 2.3, while the surface temperature field was monitored continuously using the infrared thermal imager. The results are shown in Figs. 11(b) and 11(c).

It could be observed that enlarging the effective heat transfer area significantly promoted the spatial expansion of the steam-induced thermal influence range. Compared with the intact sample, after 10 min of steam injection, the average temperatures in Regions 1 and 2 increased by 8.2 and 4.2 °C, respectively (Fig. 4(b)), while the high-temperature region expanded by 8.59%. After 90 min, the temperature increments were 6.2 and 1.5 °C, and the high-temperature region increased by 14.4%. In contrast to the superheated steam experiment, the high-temperature regions increased by 13.87% and 21.4% after 10 min and 90 min, respectively. These findings indicate that, compared to increasing the steam temperature alone, expanding the heat exchange interface was more effective in extending the thermal influence range.

In addition, a distinct asymmetry was observed between the upper and lower parts of the borehole. Compared to the lower region, the upper region consistently exhibited a larger high-temperature area. During the early stage (within 10 min), high-temperature zones developed near the lower fractures adjacent to the borehole. However, between 30 and 90 min, these regions gradually contracted, which was attributed to

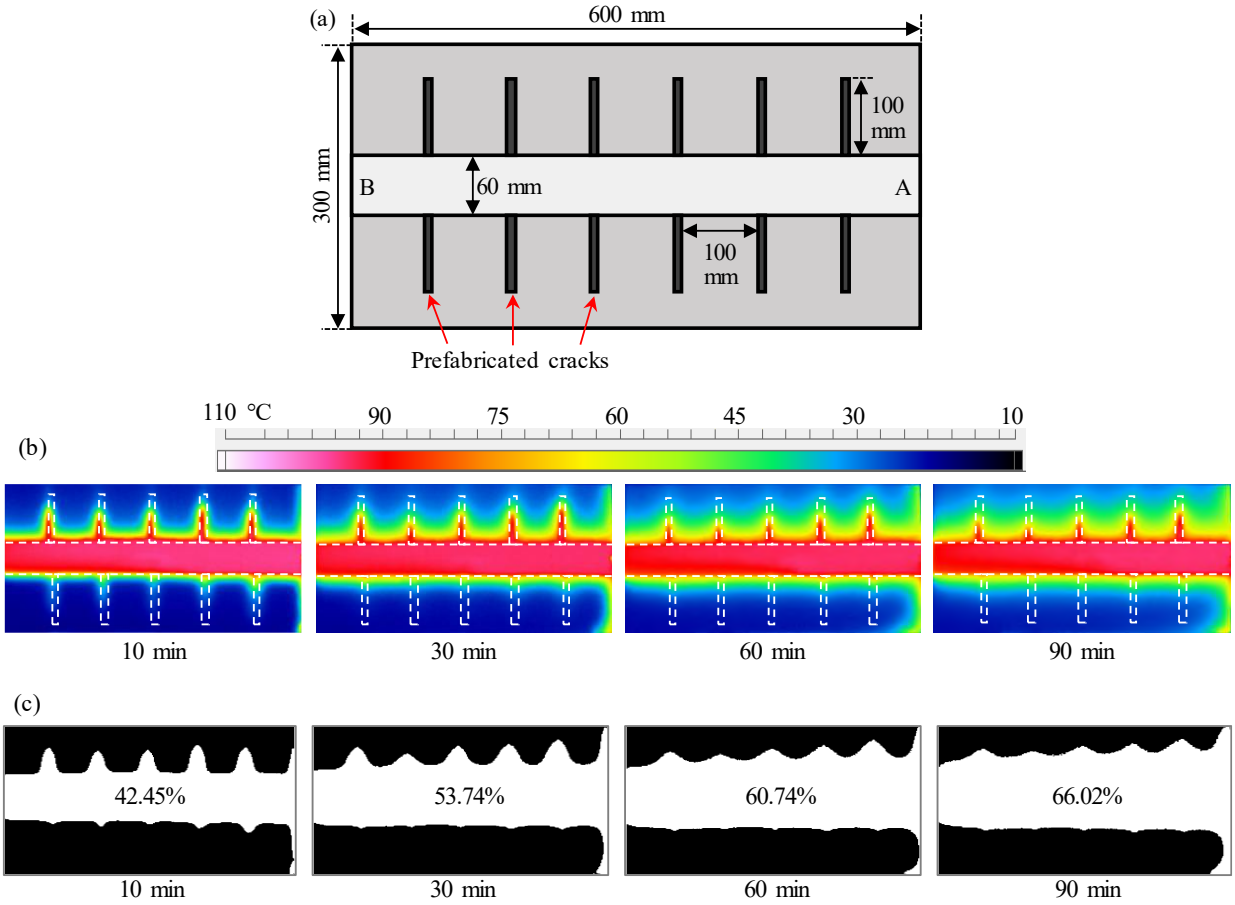

Fig. 11. (a) Schematic diagram of the sample after prefabricating cracks, changes in (b) coal surface temperature field and (c) high-temperature region at different durations of steam injection into the borehole with prefabricated cracks.

condensate accumulation. During saturated steam injection, condensation occurred along the borehole wall, and condensate progressively accumulated in the lower borehole and lower fractures under gravity. At the initial stage, when the condensate volume was limited, convective heat transfer dominated and the coal temperature increased rapidly. As injection continued, increasing the condensate thickness elevated thermal resistance and reduced heat transfer efficiency. In contrast, the upper borehole wall and fractures were less affected by liquid accumulation, allowing convection to remain the dominant mechanism and resulting in a broader high-temperature region.

The engineering implications of these findings suggest that fracture enhancement before steam injection is highly likely to increase the effective heat transfer area and expand the thermal influence zone. Meanwhile, effective condensate control should to be considered to prevent heat transfer deterioration caused by liquid accumulation during long-term injection.

4.2 Mechanism of coal deformation induced by steam injection

The experimental results presented in previous sections reveal a clear spatial correspondence between surface temperature and strain distributions during steam injection. To further interpret these observations, this section analyzes the deformation mechanism of coal from a thermoelastic perspective and provides a mechanistic explanation for the temperature-strain evolution characteristics.

The deformation of coal induced by steam injection into boreholes is a complex process influenced by multiple factors, including steam temperature, flow rate, boundary constraints, and the intrinsic physicochemical properties of coal. In the present laboratory-scale study, the dominant mechanism is considered to be thermally induced stress resulting from temperature gradients within the coal matrix.

Thermal stress refers to the stress generated within a material in the absence of external forces when thermal deformation caused by temperature variation is mechanically constrained (Boley and Weiner, 2012). In this study, during steam injection, the part of coal near the borehole wall experienced a rapid temperature rise, whereas regions farther away remained relatively cooler. This non-uniform temperature distribution generated internal temperature gradients, restricting the free thermal expansion of adjacent material elements and consequently inducing thermally generated stresses within the coal mass.

To provide a mechanical interpretation of this process, a differential element within the coal was considered for stress analysis. Fig. 12 schematically illustrates an infinitesimal hex-

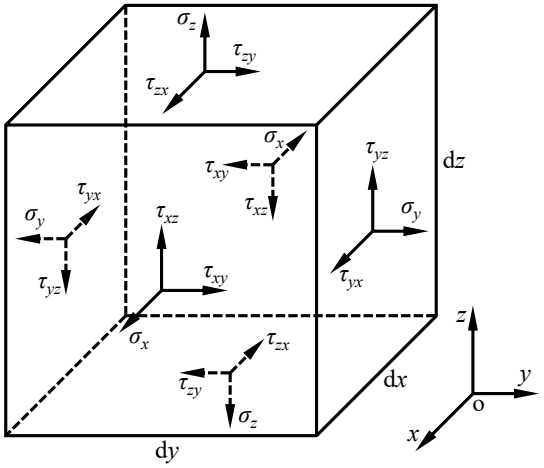

Fig. 12. Schematic diagram of stresses on the internal microelements of coal.

ahedral element with edges parallel to the coordinate axes and lengths of dx, dy and dz. The stress components acting on the faces dxdy, dxdz and dydz are denoted as (σ_z, τ_{zx}, τ_{zy}), (σ_y, τ_{yx}, τ_{yz}) and (σ_x, τ_{xy}, τ_{xz}), respectively, satisfying $\tau_{xy} = \tau_{yx}$, $\tau_{xz} = \tau_{zx}$, $\tau_{yz} = \tau_{zy}$.

For simplicity, coal is treated as an equivalent isotropic, linear elastic medium. Although natural coal exhibits heterogeneity and anisotropy due to bedding planes and fracture systems, the observed deformation in this study remained within the small-strain range (maximum strain $\approx 0.3\%$), and no macroscopic damage was detected. Therefore, the classical thermoelastic framework provides a first-order approximation that is reasonable for qualitative interpretation.

Under free expansion conditions, when the temperature of the element changes from t_1 to t_2, the strain components of an isotropic material are expressed as $\varepsilon_{ox} = \varepsilon_{oy} = \varepsilon_{oz} = \alpha(t_2 - t_1)$, where α denotes the coefficient of thermal expansion. However, under constrained conditions, thermal stresses develop. According to the linear thermoelastic theory, the total strain comprises thermal strain and elastic strain induced by stress. Extending Hooke's law yields the following strain equations (Boley and Weiner, 2012):

$$\begin{aligned}
\varepsilon_x &= \alpha(t_2 - t_1) + \frac{1}{E}\left[\sigma_x - \mu\left(\sigma_y + \sigma_z\right)\right] \\
\varepsilon_y &= \alpha(t_2 - t_1) + \frac{1}{E}\left[\sigma_y - \mu\left(\sigma_x + \sigma_z\right)\right] \\
\varepsilon_z &= \alpha(t_2 - t_1) + \frac{1}{E}\left[\sigma_z - \mu\left(\sigma_x + \sigma_y\right)\right]
\end{aligned} \tag{6}$$

where ε_x, ε_y, and ε_z denote the strains in the ox, oy and oz directions, respectively; t_1 and t_2 are the temperatures of the element before and after changing; E is the elastic modulus, μ is Poisson's ratio, and σ_x, σ_y, and σ_z are the thermal stresses in the respective directions.

These relationships indicate that strain magnitude at a given location is primarily governed by local temperature variation and material elastic properties. The experimentally observed spatial consistency between temperature and strain fields supports this thermoelastic mechanism: Regions experiencing larger temperature gradients developed correspondingly higher strain levels.

It should be noted that under field conditions, additional factors such as formation stress changes and pore pressure variations may influence coal deformation by altering effective stress. However, pore pressure evolution was not directly measured or modeled in this laboratory study, which rather focuses on thermally induced elastic deformation under controlled experimental conditions.

4.3 Heat transfer mechanism of saturated steam in coal boreholes

During the injection of saturated steam into a horizontal borehole, the internal flow behavior directly influences the convective heat transfer intensity and thus affects the overall heat transfer efficiency. Therefore, it is necessary to first analyze the steam flow regime to better understand the subsequent temperature evolution characteristics observed in the experiments.

Because the borehole diameter (60 mm) was much larger than the steam outlet diameter (5 mm), steam underwent sudden expansion upon entering the borehole. Under simplified single-phase assumptions, the local flow condition near the injection outlet could be preliminarily estimated using the Reynolds number. For a steam flow rate of 100 mL/min at 100 °C, the calculated Reynolds number is approximately 19, which is significantly lower than the critical value of 2000 for pipe flow. This suggests that the flow immediately near the outlet may have initially exhibited laminar characteristics.

However, this estimation is only valid for the near-outlet region under idealized assumptions. In the actual borehole environment, several additional factors significantly alter the flow structure. First, steam expansion into the larger cavity induces velocity redistribution and flow instability. Second, the sealed end of the borehole generates backflow when the injected steam reaches the terminal boundary, leading to interaction between incoming and returning streams. Third, due to density differences between steam and air, buoyancy effects promote the upward accumulation of steam, resulting in asymmetric flow distribution. Finally, condensation occurring at the borehole wall produces a confined two-phase flow system consisting of steam and liquid condensate.

To better illustrate the temporal evolution of these complex flow structures within the borehole, a schematic diagram has been provided for clarification. As shown in Fig. 13, at the initial stage (Fig. 13(a)), steam propagates primarily along the borehole axis. Upon contacting the borehole wall and reaching the sealed end (Fig. 13(b)), reflected flow and vortical structures begin to develop. With continued injection (Fig. 13(c)), the borehole becomes largely filled with steam, and a complex recirculating motion is established throughout the cavity.

Our experimental observations indicated that steam began escaping from the open end within approximately one minute after injection, while the total injection duration lasted about 90 minutes. Therefore, although the Reynolds number suggests laminar conditions locally at the injection outlet during the very early stage, the overall borehole flow during most of the injection process can be characterized as a confined, non-

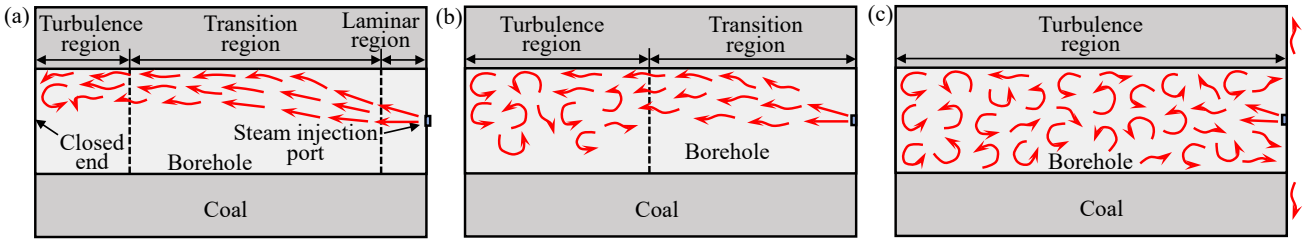

Fig. 13. Schematic diagram of transient flow behavior in the borehole during steam injection: (a) Initial stage, (b) time at which the steam front reaches the sealed end and (c) fully steam-filled condition.

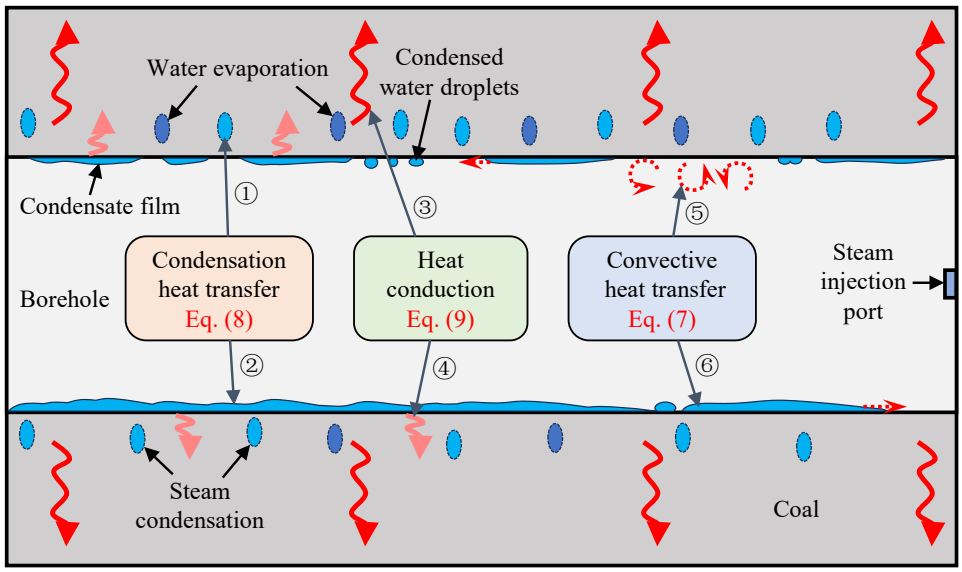

Fig. 14. Schematic diagram of heat transfer modes after injecting saturated steam into the borehole for a period. ① Steam condensation in coal; ② Steam condensation in the borehole; ③ Intrinsic thermal conduction of coal; ④ Thermal conduction of condensate film; ⑤ Flow of steam; ⑥ Movement of condensate film.

uniform, two-phase turbulent regime. This turbulent mixing enhances convective heat transfer by increasing the effective heat transfer coefficient and promoting more intensive thermal exchange between steam and the borehole wall.

Heat transfer involves three fundamental mechanisms: Conduction, convection and radiation (Naterer, 2021). On this basis, heat transfer during steam injection can be considered as the combined effects of convective heat transfer, condensation heat transfer and heat conduction (Fig. 14). Radiative heat transfer is proportional to the fourth power of absolute temperature. Given that the experimental temperatures (100 ~ 200 °C) were relatively moderate, radiative effects were negligible compared with convection and condensation and were therefore not considered.

(1) Convective heat transfer

Convective heat transfer refers to the transfer of heat caused by macroscopic fluid motion resulting from temperature-induced mixing (Naterer, 2021). In the present system, as soon as turbulent flow developed within the borehole, convective heat transfer became an important mechanism for transferring sensible heat from steam to the borehole wall.

The rate of convective heat transfer can be expressed according to Newton's law of cooling (Nandagopal, 2023):

$$Q_l = h_l A_l \Delta T_l \tag{7}$$

where Q_l denotes the convective heat transfer capacity, h_l denotes the convective heat transfer coefficient, A_l denotes the heat transfer area, and ΔT_l denotes the temperature difference between the steam and the borehole wall.

Because turbulent flow significantly increases h_l, the transition from local laminar conditions to a global turbulent regime plays a crucial role in determining the overall heating efficiency.

(2) Condensation heat transfer

When saturated steam contacts a surface whose temperature is lower than its saturation temperature, phase change occurs and latent heat is released. This condensation heat transfer is a specialized form of convection and is generally much more efficient than pure convective heat transfer because of the large latent heat of vaporization. In our experiment, condensation primarily occurred at the interface between steam and the borehole wall, while only a limited amount of steam penetrated pores and fractures within the coal matrix and condensed internally. The condensation heat transfer can be expressed as:

$$Q_n = h_n A_n \Delta T_n \tag{8}$$

where Q_n represents the condensation heat transfer capacity, h_n denotes the condensation heat transfer coefficient, A_n denotes the heat transfer area, and ΔT_n represents the temperature difference between the steam and the wall or the interior of the coal. Typically, h_n is substantially greater than h_l due to latent heat release during phase change.

Two condensation modes are generally recognized: Filmwise condensation and dropwise condensation. Although the latter can provide heat transfer coefficients $5 \sim 10$ times higher than the former (Nandagopal, 2023), visual observation in this experiment indicated that filmwise condensation predominated along the borehole wall.

(3) Heat conduction

Heat conduction occurs within stationary media through molecular interaction. In this system, conduction primarily took place through two primary pathways: Heat transfer from the condensate layer to the borehole wall, and thermal diffusion from the heated borehole wall into the surrounding coal matrix. The heat conduction capacity can be expressed as:

$$Q_d = -k_d A_d \frac{\Delta T_d}{\Delta x_d} \tag{9}$$

where Q_d represents the heat conduction capacity, k_d denotes the thermal conductivity of the condensate or coal, A_d denotes the contact area, ΔT_d is the temperature difference, and Δx_d denotes the distance of heat transfer.

Based on our experimental observations, the overall heat transfer process during saturated steam injection can be divided into three stages:

1) Initial stage: Condensation begins immediately upon steam contact with the relatively cool borehole wall, releasing latent heat and forming a non-uniform condensate layer. In areas not yet covered by condensate, convective heat transfer dominates, raising the wall temperature. A limited amount of steam penetrates coal micro-pores and fractures and condenses internally.
2) Intermediate stage: As injection continues, the borehole wall temperature increases and the condensate layer thickens, particularly along the lower side due to gravity. Heat is conducted from the wall into the surrounding coal matrix. Steam flow might entrain portions of condensate, leading to simultaneous convection and conduction processes. Spatially non-uniform condensate distribution results in heterogeneous heat transfer intensity.
3) Late stage: With further heating and subsequent temperature rise, moisture within the coal and part of the accumulated condensate might re-evaporate, while condensation continues in cooler regions. The coexistence of condensation and evaporation creates a dynamically evolving two-phase heat transfer system. Regions without complete condensate coverage continue to experience convective exchange.

In general, heat transfer during steam injection into coal boreholes is governed by the coupled effects of turbulent convection, phase-change heat transfer, and thermal conduction. While condensation provides substantial latent heat release, turbulent flow enhances convective heat transfer and promotes more uniform energy distribution within the borehole cavity. Convective mixing and phase change processes dominate the initial and intermediate thermal responses, while conduction into the coal matrix governs longer-term thermal diffusion.

Because the above process involves confined geometry, buoyancy effects, two-phase flow, and spatially varying condensate thickness, quantitatively predicting the total heat transfer remains challenging. Nevertheless, understanding the dominant mechanisms and their interactions provides a more systematic interpretation of the experimentally observed temperature field evolution and offers a theoretical basis for optimizing steam injection strategies and improving thermal efficiency in coal seam applications. By selecting appropriate injection parameters, borehole configurations and condensate management strategies, the effective thermal influence range can be expanded, thereby enhancing CBM recovery and energy utilization efficiency.

5. Conclusions

1) During steam injection into the horizontal borehole, coal surface temperature increases rapidly before reaching a quasi-steady state. The upper region consistently exhibits higher temperatures than the lower region due to buoyancy-driven steam redistribution. Increasing the steam flow rate from 50 to 150 mL/min and temperature from 100 to 200 °C slightly expands the high-temperature zone, whereas enlarging the effective heat transfer area significantly increases the thermal influence range.
2) For saturated steam at 100 °C, latent heat transfer dominates, resulting in relatively uniform temperature distribution and higher heat transfer efficiency. In contrast, superheated steam (200 °C) is governed mainly by sensible heat transfer, leading to more localized heating near the injection end and stronger spatial temperature gradients.
3) Steam injection induces a measurable thermoelastic response on the coal surface. After 90 min of injection at 200 °C, the maximum surface strain reaches about 0.3%, while the average strain remains below 0.08%. A clear spatial correspondence between temperature and strain fields was observed, indicating that deformation is primarily governed by thermally induced stress.
4) Condensate accumulation reduces local heat transfer efficiency, particularly along the lower borehole wall. Therefore, implementing an effective condensate drainage strategy is recommended for field applications. Integrating steam injection with reservoir stimulation techniques may further expand the effective heat transfer range and improve CBM recovery efficiency.

Acknowledgements

This work was supported by the Natural Science Foundation of Sichuan Province (No. 2024NSFSC0971), the Special Support for Postdoctoral Research Projects in Sichuan Province (No. TB2024056), and the Scientific Research Foun-

dation of Xihua University (No. Z211014).

Conflicts of interest

The authors declare no competing interest.

References

Alarawi, A., Busaleh, A., Saleh, T. A., et al. High thermal stability of foams stabilized by graphene oxide and zwitterionic surfactant nanocomposites for fracturing applications. Fuel, 2023, 332: 126156.

Boley, B. A., Weiner, J. H. Theory of Thermal Stresses. New York, USA, Dover Publications, 2012.

Feng, J., Qiu, H., Zhang, P., et al. From single-interface LN_2 fracturing to CBM stimulation: Temperature optimization and cracking mechanism. Fuel, 2026, 408: 137691.

Flores, R. M. Coalbed methane: From hazard to resource. International Journal of Coal Geology, 1998, 35(1-4): 3-26.

Gong, H., Yu, C., Jiang, Q., et al. Improving recovery efficiency by CO_2 injection at late stage of steam assisted gravity drainage. Advances in Geo-Energy Research, 2022, 6(4): 276-285.

Gunter, W. D., Gentzis, T., Rottenfusser, B. A., et al. Deep coalbed methane in Alberta, Canada: A fuel resource with the potential of zero greenhouse gas emissions. Energy Conversion and Management, 1997, 38: S217-S222.

Hassan, G. M. Deformation measurement in the presence of discontinuities with digital image correlation: A review. Optics and Lasers in Engineering, 2021, 137: 106394.

Heinze, T., Pastore, N. Velocity-dependent heat transfer controls temperature in fracture networks. Nature Communications, 2023, 14(1): 362.

Hu, L., Feng, Z., Zhou, D. Theory and engineering practice of intermittent heat injection-enhanced coalbed methane extraction. ACS Omega, 2023, 8(42): 39625-39635.

Jarrahi, M., Moore, K. R., Holländer, H. M. Comparison of solute/heat transport in fractured formations using discrete fracture and equivalent porous media modeling at the reservoir scale. Physics and Chemistry of the Earth, Parts A/B/C, 2019, 113: 14-21.

Lan, W., Wang, H., Liu, Q., et al. Investigation on the microwave heating technology for coalbed methane recovery. Energy, 2021, 237: 121450.

Li, W., Yang, X., Zhang, Y., et al. Experimental study on migration yield law of coal-bed methane under the condition of saturated steam. Journal of China Coal Society, 2018, 43(5): 1343-1349. (in Chinese)

Li, Y., Ji, H., Li, G., et al. Effect of supercritical CO_2 transient high-pressure fracturing on bituminous coal microstructure. Energy, 2023, 282: 128975.

Li, Y., Zhai, C., Xu, J., et al. Feasibility investigation of enhanced coalbed methane recovery by steam injection. Energy, 2022, 255: 124473.

Liang, H., Chu, X., Zheng, J., et al. Study on the evolution and damage law of coal microstructure under the effect of temperature rise during heat injection. International Communications in Heat and Mass Transfer, 2025a, 169: 109616.

Liang, Y., Yang, K., Yang, Z., et al. Hydro-mechanical-damage coupling effect of hydraulic fracturing in fractured dual-medium coal masses. Computers and Geotechnics, 2025b, 178: 106909.

Liu, T., Wang, J., Lin, B., et al. Numerical simulation on enhanced coalbed methane extraction by hot flue gas based on the ECM-DFM model. Computers and Geotechnics, 2025, 184: 107253.

Liu, Y., Lin, B., Liu, T., et al. Numerical analysis on the coupling of transient fluid flow and heat transfer within the complex fracture network of coal based on 3D reconstruction of CT images. International Communications in Heat and Mass Transfer, 2024, 159: 108217.

Liu, Y., Lin, B., Liu, T., et al. Study on the micro conjugate heat transfer characteristics of coal reconstructed from CT images under the influence of temperature. Fuel, 2023, 349: 128643.

Longinos, S. N., Begaliyev, D., Asif, M., et al. Cryogenic fracturing of coal with LN_2 treatment: A sustainable approach for enhancing coalbed methane extraction in water-scarce regions. Gas Science and Engineering, 2025, 142: 205686.

Ma, R., Zhang, J., Feng, Q., et al. Effect of cyclic hydraulic stimulation on pore structure and methane sorption characteristics of anthracite coal: A case study in the Qinshui Basin, China. Petroleum Science, 2024, 21(5): 3271-3287.

Mallick, N., Prabu, V. Energy analysis on Coalbed Methane (CBM) coupled power systems. Journal of CO_2 Utilization, 2017, 19: 16-27.

Megía, P. J., Vizcaíno, A. J., Calles, J. A., et al. Hydrogen production technologies: From fossil fuels toward renewable sources. A mini review. Energy & Fuels, 2021, 35(20): 16403-16415.

Mezon, C., Mourzenko, V. V., Thovert, J. F., et al. Thermal convection in three-dimensional fractured porous media. Physical Review E, 2018, 97(1): 013106.

Moore, T. A. Coalbed methane: A review. International Journal of Coal Geology, 2012, 101: 36-81.

Nandagopal, N. S. Chemical Engineering Principles and Applications. Bengaluru, India, Springer, 2023.

Naterer, G. F. Advanced Heat Transfer. Boca Raton, USA, CRC Press, 2021.

Nie, B. Development of low-metamorphic coalbed methane reservoirs with superheated steam injection: Simulation of wellbore heat transfer. Energy, 2023, 275: 127461.

Pashin, J. C., McIntyre, M. R. Temperature-pressure conditions in coalbed methane reservoirs of the Black Warrior basin: Implications for carbon sequestration and enhanced coalbed methane recovery. International Journal of Coal Geology, 2003, 54(3-4): 167-183.

Qiu, L., Wang, S., Hu, B., et al. A review on high-value development and utilization of unconventional methane-

containing gaseous fuel resources. Energy Conversion and Management, 2024, 319: 118980.

Shahtalebi, A., Khan, C., Dmyterko, A., et al. Investigation of thermal stimulation of coal seam gas fields for accelerated gas recovery. Fuel, 2016, 180: 301-313.

Talapatra, A., Halder, S., Chowdhury, A. I. Enhancing coal bed methane recovery: Using injection of nitrogen and carbon dioxide mixture. Petroleum Science and Technology, 2021, 39(2): 49-62.

Tang, X., Fu, X., Zou, J., et al. Responses of physico-chemical properties and CH_4 adsorption/desorption behaviors of diverse rank coal matrices to microwave radiation. Gas Science and Engineering, 2024, 128: 205359.

Teng, T., Zhao, Y., Gao, F., et al. A fully coupled thermo-hydro-mechanical model for heat and gas transfer in thermal stimulation enhanced coal seam gas recovery. International Journal of Heat and Mass Transfer, 2018, 125: 866-875.

Verdugo, M., Doster, F. Impact of capillary pressure and flowback design on the clean up and productivity of hydraulically fractured tight gas wells. Journal of Petroleum Science and Engineering, 2022, 208: 109465.

Wang, X., Meng, Z., Zhang, K. Experimental study on methane adsorbed-phase density, adsorption capacity and thermodynamic mechanism of anthracite coal under deep temperature and pressure conditions. Journal of Environmental Chemical Engineering, 2025, 13(3): 116366.

Wang, Z., Kieu, H., Nguyen, H., et al. Digital image correlation in experimental mechanics and image registration in computer vision: Similarities, differences and complements. Optics and Lasers in Engineering, 2015, 65: 18-27.

Wei, Z., Sheng, M., Li, J., et al. Pressure diagnostics in hydraulic fracturing for unconventional completion optimization. Advances in Geo-Energy Research, 2025, 17(3): 196-211.

Yang, K., Liang, Y., Li, Q., et al. A coupled thermo-hydro-mechanical damage (THMD) model based on finite element method-discrete fracture model (FEM-DFM) for simulating supercritical CO_2 ($ScCO_2$) fracturing. Computers and Geotechnics, 2026, 191: 107795.

Yuan, R., Chen, C., Wei, X., et al. Heat-fluid-solid coupling model for gas-bearing coal seam and numerical modeling on gas drainage promotion by heat injection. International Journal of Coal Science & Technology, 2019, 6(4): 564-576.

Zhang, B., Tao, S., Yang, F., et al. The genesis and accumulation mechanism of CBM in the typical mid-to low-rank coal-bearing basins. Petroleum Science, 2025, 22(8): 3069-3085.

Zhang, L., Hascakir, B. A review of issues, characteristics, and management for wastewater due to hydraulic fracturing in the US. Journal of Petroleum Science and Engineering, 2021, 202: 108536.

Zhao, D., Li, X., Feng, Z., et al. Study on the behavior and mechanism of methane desorption-diffusion for multi-scale coal samples under multi-temperature conditions. Fuel, 2022, 328: 125332.

Zheng, C., Liu, S., Han, F., et al. Experimental investigation of the effect of microstructure on coalbed methane adsorption characteristics affected by chemical solvents. Langmuir, 2025a, 41(1): 774-786.

Zheng, Y., Zhai, C., Chen, A., et al. Effect of pulsation frequencies on the fracture characteristics of CO_2 foam fractured coal: An experimental study. Gas Science and Engineering, 2025b, 141: 205668.